Progress In Electromagnetics Research, Vol. 148, 1–14, 2014

Analysis of Moving Human Micro-Doppler Signature in Forest Environments

Jose M. Garcia-Rubia*, Ozlem Kilic, Vinh Dang, Quang Nguyen, and Nghia Tran

Abstract—Automatic detection of human motion is important for security and surveillance applications. Compared to other sensors, radar sensors present advantages for human motion detection and identification because of their all-weather and day-and-night capabilities, as well as the fact that they detect targets at a long range. This is particularly advantageous in the case of remote and highly cluttered radar scenes. The objective of this paper is to investigate human motion in highly cluttered forest medium to observe the characteristics of the received Doppler signature from the scene. For this purpose we attempt to develop an accurate model accounting for the key contributions to the Doppler signature for the human motion in a forest environment. Analytical techniques are combined with full wave numerical methods such as Method of Moments (MoM) enhanced with Fast Multipole Method (FMM) to achieve a realistic representation of the signature from the scene. Mutual interactions between the forest and the human as well as the attenuation due to the vegetation are accounted for. Due to the large problem size, parallel programming techniques that utilize a Graphics Processing Unit (GPU) based cluster are used.

1. INTRODUCTION

A capability to detect, track and monitor human motion in highly cluttered environments, such as forests, is important for security and surveillance operations. Particularly for border control applications, it is essential to track and classify humans moving in remote locations over a long period of time, at a low cost, and with low maintenance. Several different radio-frequency devices have been developed for this purpose; in particular Doppler radars are widely used for human discrimination applications [1, 2].

Human movement can be classified by using micro-Doppler radar systems that are capable of detecting small variations in the carrier frequency caused by motion. Studies have shown that the human micro-Doppler signature is a unique signature, differentiable from all other micro-Doppler signatures, including those caused by four-legged animals [3, 4]. The micro-Doppler frequency shift depends on the transmitted frequency and the velocity of the different body parts over time [5–8]. This has been exploited for identification and classification of different human activities [9]. To analyze the micro-Doppler signatures, a joint time-frequency transform such as the Short-Time Fourier Transform (STFT) is performed. Different types of motions can be identified and classified from micro-Doppler spectrograms [9, 10].

Most of the recent research in this field have focused on using continuous wave (CW) radar for Doppler detection due to their simpler system design and implementation, and lower development cost. For example, a CW microwave Doppler radar operating at 2.4 GHz was developed for multiple-mover sensing [11]. CW microwave Doppler radars have been widely used for vital sign detection and life

---

Received 23 January 2014, Accepted 21 May 2014, Scheduled 15 June 2014

* Corresponding author: Jose Miguel Garcia-Rubia (garciarubia@cua.edu).

The authors are with the Department of Electrical Engineering and Computer Science, The Catholic University of America, 620 Michigan Ave., N.E., DC 20064, USA.

detection [12–15], and for extracting the Doppler signatures for biometric characterization [16]. Signal processing and Doppler extraction method for CW Doppler radar were also discussed in [4, 17–22].

The objective of this paper is to investigate human motion in a highly cluttered forest medium to observe the characteristics of the received Doppler signature from the scene. We present the results of an accurate model which accounts for the key contributions to the Doppler signature of the human motion in a forest environment.

A CW radar is assumed to generate a plane wave that is incident on the scene. The incident wave is attenuated as it propagates through the forest based on reported specific attenuation values for wooded areas [23]. Human motion is created within the scene to analyze the received signature characteristics. The backscattered fields at the radar are calculated from the contributions of the forest and the human in motion accounting for the first-order mutual coupling effects between the forest and the human. The forest scattering model represents the trees as PEC cylinders distributed randomly over a flat ground, and employs a first-order approximation where the contributions from each tree are summed independently. A full wave technique, namely Method of Moments enhanced with Fast Multipole Method (MoM-FMM), is employed to accurately model the scattered fields from the human in motion since this is the main term which contributes to the Doppler signature. The mutual coupling between human and the forest can also contribute to the information about the human in motion, and is included in the model.

The rest of the paper is organized as follows. In Section 2, the human walking model based on empirical data is presented. The scattering models for the human and forest are explained in Section 3. The micro-Doppler radar spectrograms are presented in Section 4. The simulation results for various test case scenarios are presented in Section 5. Finally, the conclusions are summarized in Section 6.

2. HUMAN WALKING MODEL

Realistic human motion models have been investigated by many authors. Some of these models are obtained from real motion capture data [24]. However such data is limited to specific parameters from the captured scene such as the particular direction, speed, and human characteristics. In order to study different human motion effects, we opt to use a standard analytical model extracted from empirical data, such as the well-known Boulic model [25–28].

According to the Boulic model, the human body can be described by 16 joints, which are identified by the small circles as shown in Figure 1. The body parts are defined by two joints at each end; e.g., foot is defined by the toe and the ankle. The 17 body parts are depicted by the head and the lines between the joints as depicted in Figure 1. Each body part is modeled using ellipsoids with different semi-axes lengths appropriate for the corresponding body part. The motion is described using the Boulic walking model based on time-dependent translations and rotations of each joint [25]. The input variables for this model are the velocity and the height of the human. Given these two inputs, the human is created, and motion characteristics are defined, as shown in Figure 1.

The motion is characterized by cycles that repeat for a constant velocity. Each cycle carries features due to the relative motion of the various joints and body parts. The next position and orientation of a body part in the cycle is calculated using 3 translations and 14 rotation trajectories, five of which are duplicated for both sides of the body. The details of the motion parameters are listed in Table 1 where

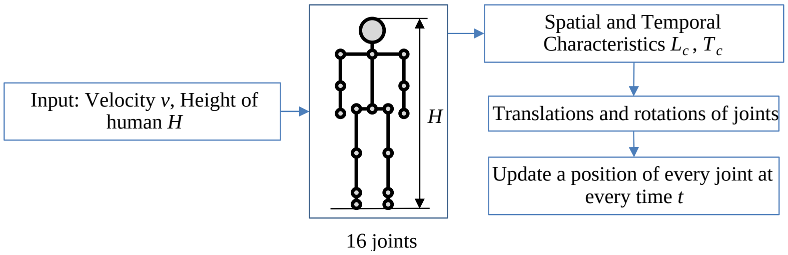

Figure 1. Human motion model with 17 body parts, 3 translation trajectories and 14 rotation trajectories.

Table 1. Body trajectories.

	Translation (m)	**Body rotation (deg)**	**Left rotation (deg)**	**Right rotation (deg)**
General				
Vertical Translation	$T_V(t)$			
Lateral Translation	$T_L(t)$			
Forward/Backward Translation	$T_{FB}(t)$			
Lower body				
Rotation at Ankle			$\varphi_A(t)$	$\varphi_A(t+0.5)$
Rotation at Knee			$\varphi_K(t)$	$\varphi_K(t+0.5)$
Rotation at Hip			$\varphi_H(t)$	$\varphi_H(t+0.5)$
Rotation Left/Right		$\varphi_{LR}(t)$		
Rotation Torsion		$\varphi_{TO}(t)$		
Upper body				
Rotation at Elbow			$\varphi_E(t)$	$\varphi_E(t+0.5)$
Rotation at Shoulder			$\varphi_S(t)$	$\varphi_S(t+0.5)$
Rotation Forward/Backward		$\varphi_{FB}(t)$		
Rotation Thorax		$\varphi_{TH}(t)$		

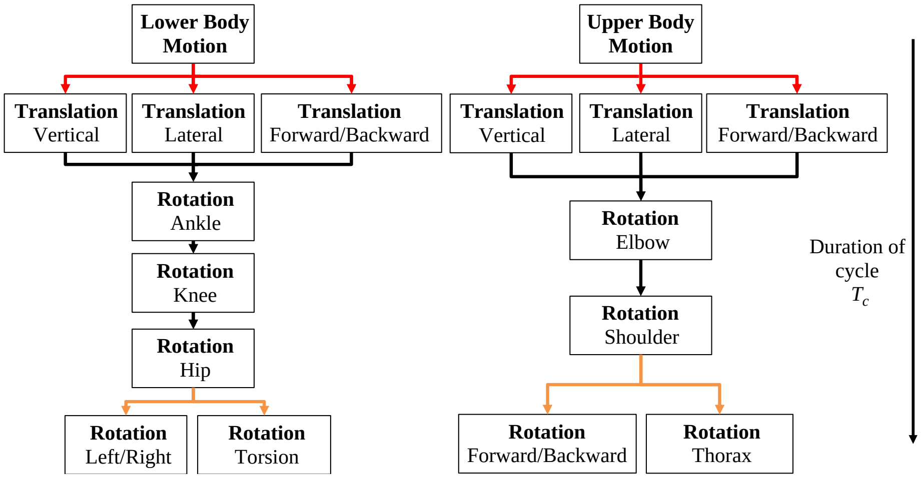

Figure 2. Lower and upper body motion.

t is the relative time with respect to the duration of the cycle, T_c. All the translations and rotations are dependent on the fundamental spatial and temporal characteristics of the motion such as the relative length, L_c, and the duration of the walking cycle, T_c.

The fundamental spatial characteristic of the human walk in the Boulic model is the relative length of the walking cycle, L_c, which depends on the relative velocity, R_v, such that $L_c = 1.346\sqrt{R_v}$. The relative velocity is defined as the average walking velocity normalized by the height of the thigh, which is approximately 50% of the height of the human. The fundamental temporal characteristic of the Boulic model is the duration of cycle, T_c, which is a ratio of the relative length of walking cycle to the relative velocity; i.e., $T_c = L_c/R_v$. These spatial and temporal characteristics are utilized to calculate the various translations and rotations of each body part as listed in Table 1 [25].

The translations and rotations are applied for the lower and the upper parts of the body as depicted

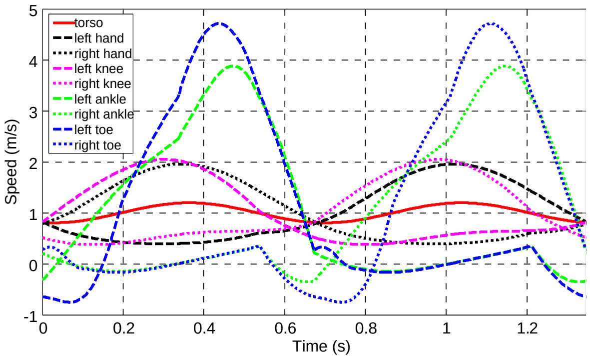

Figure 3. Radial velocities for different body joints in one cycle.

in Figure 2. For example, to define the trajectory of one part of the lower body, 3 translations (vertical, lateral, and forward/backward) are applied to all joints. Then three rotation motions are applied in sequence, starting with the ankle, continuing with the knee and finishing with the hip. Finally the two rotations left/right and torsion are applied to all lower body joints. The joints' trajectories for the upper part of the body are calculated in an analogous way.

According to this model, a human with a height of 1.8 m, moving at 0.9 m/s has a walking cycle period, $T_c = 1.346\,\mathrm{s}$. The radial velocities for different body joints are shown for a single walking cycle period in Figure 3. The lower part of the legs presents the maximum velocity over the cycle, while the torso depicts a velocity with very low oscillations around the velocity of the translational movement of the human.

3. RADAR SCATTERING MODEL

A continuous wave (CW) microwave radar is assumed to generate a plane wave, E_0, that is incident on the scene. The forest is modeled with PEC cylinders representing the trunks over a flat PEC ground, as shown in Figure 4. The incident wave attenuates as it propagates through the forest. The attenuation inside the medium is assumed constant for all directions based on the reported specific attenuation values for wooded areas at frequencies above 1 GHz [23]. Three contributions from the scene, as depicted in Figure 4 by $E_{f\text{-}r}$, $E_{h\text{-}r}$ and $E_{f\text{-}h\text{-}r}$, are considered for the calculation of the total backscattered fields from the scene.

The first term, $E_{f\text{-}r}$, is the direct contribution from the forest to the radar, which involves a first-order analytical approach accounting for the reflections from the ground. The second term, $E_{h\text{-}r}$, is the contribution from the human, which employs the MoM-FMM full wave method. Ground reflections and mutual coupling effects between the different body parts are accounted for in this term. The third contribution, $E_{f\text{-}h\text{-}r}$, accounts for the first-order interactions between the forest and human by calculating the incident fields on the human as a result of radiated fields from all trees in the forest. The

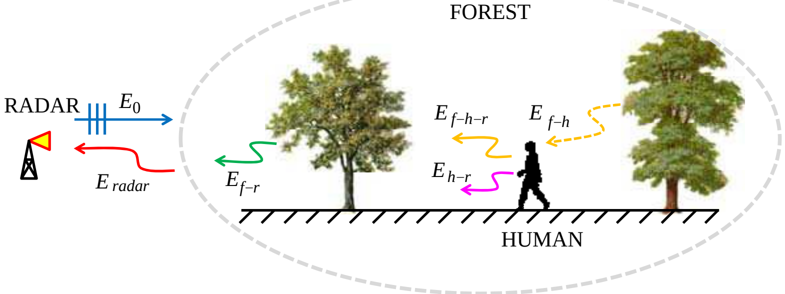

Figure 4. Contributions to radar signature from the scene.

other mutual coupling term, i.e., the illumination of the forest due to radiated fields from the human is considered negligible compared to $E_{f\text{-}h\text{-}r}$. As in the calculation of $E_{f\text{-}r}$ and $E_{h\text{-}r}$, the reflection from the ground and attenuation effects are included in $E_{f\text{-}h\text{-}r}$. The fields at the radar, E_{radar}, are calculated as the sum of these three terms, as in (1).

$$E_{radar} = E_{f\text{-}r} + E_{h\text{-}r} + E_{f\text{-}h\text{-}r} \tag{1}$$

A description of the modeling approach for these three terms is provided below.

3.1. Forest to Radar Scattering, $E_{f\text{-}r}$

Electromagnetic scattering from the forest is an important remote sensing problem for agricultural and environmental purposes [29, 30]. For the microwave radar frequencies considered in this paper, the trunks in a typical forest are separated by multiple wavelengths. Consequently, the received fields at the radar can be estimated by using a first-order approximation.

We employ an analytical approach, where the trees are modeled as finite length, PEC cylinders residing vertically over a flat PEC ground as in [31, 32]. The cylinders can be of various sizes, and are randomly distributed over the ground. We consider a plane wave illumination on the forest while accounting for attenuation as the wave propagates inside the medium, as shown in Figure 5. The attenuation inside the medium is assumed constant for all directions based on the reported specific attenuation values for wooded areas at microwave frequencies [23].

Based on this approach, the total scattered field from the forest is calculated as in (2).

$$\begin{aligned}
\bar{E}_{f\text{-}r}(\bar{r}) = \frac{e^{-jkr}}{r} \sum_{j=1}^{N} \frac{L_j}{2\pi} e^{-j\bar{k}_{d\rho}\cdot\bar{\rho}_j} \Bigg\{ & \text{sinc}\left[(k_{iz}+k_{sz})\frac{L_j}{2}\right] \bar{f}_{dd}\left(\hat{k}_s, \hat{k}_i\right) e^{jk_{sz}\cdot z_j} e^{jk_{iz}\cdot z_j}\ e^{-\alpha D_j^{dd}} \\
& + \text{sinc}\left[(k_{iz}-k_{sz})\frac{L_j}{2}\right] \bar{f}_{dr}\left(\hat{k}_s, \hat{k}_i\right) e^{jk_{sz}\cdot z_j + jk_{iz}\cdot z_j} e^{-2jk_{sz}(z_j+d)} e^{-\alpha D_j^{dr}} \\
& + \text{sinc}\left[(k_{iz}-k_{sz})\frac{L_j}{2}\right] \bar{f}_{rd}\left(\hat{k}_s, \hat{k}_i\right) e^{-jk_{iz}\cdot z_j + jk_{sz}\cdot z_j - 2jk_{iz}d} e^{-\alpha D_j^{rd}} \\
& + \text{sinc}\left[(k_{iz}+k_{sz})\frac{L_j}{2}\right] \bar{f}_{rr}\left(\hat{k}_s, \hat{k}_i\right) e^{-jk_{sz}\cdot z_j} e^{-jk_{iz}\cdot z_j} e^{-2j(k_{iz}+k_{sz})d} e^{-\alpha D_j^{rr}} \Bigg\},
\end{aligned} \tag{2}$$

where N is the number of cylinders, L_j the height for each cylinder, k the wavenumber, and α the forest specific attenuation coefficient. $\hat{k}_i$ and $\hat{k}_s$ are the incidence and scattering directions, respectively. $\bar{f}_{dd}$, $\bar{f}_{dr}$, $\bar{f}_{rd}$, $\bar{f}_{rr}$ are field vectors as defined in [32], and D_j^{dd}, D_j^{dr}, D_j^{rd}, D_j^{rr} are the path lengths inside the forest corresponding to these field vectors, respectively as shown in Figure 6.

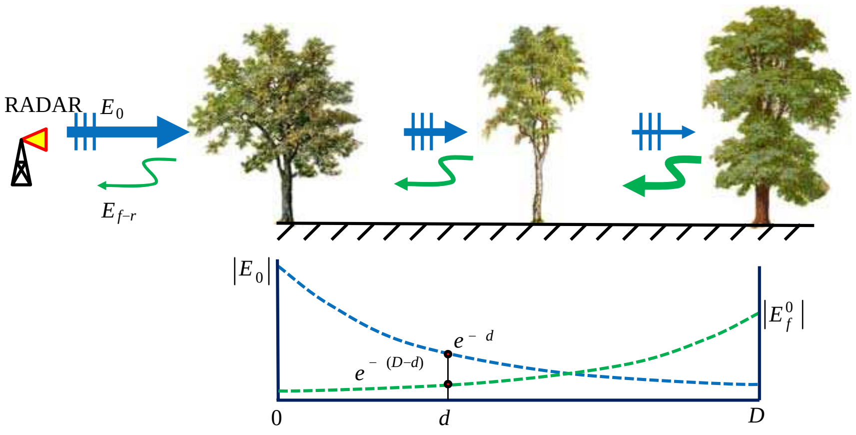

Figure 5. Forest contribution to radar signature.

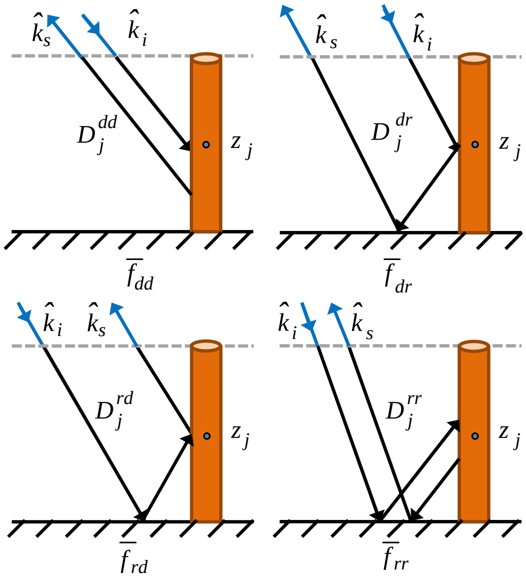

Figure 6. Four scattering contributions from the trunks in the presence of ground.

The first term shown in Figure 6, $\bar{f}_{dd}$, is the direct scattering term which involves the backscattered fields from the trunk directly towards the radar. The second and third terms, $\bar{f}_{dr}$ and $\bar{f}_{rd}$, include a single reflection from the ground. The last term, $\bar{f}_{rr}$, includes two ground reflections before the scattered fields reach the radar.

3.2. Human to Radar Scattering, $E_{h\text{-}r}$

The scattering phenomenon in human motion studies has been conventionally modeled using the simplistic concept of point scatters. In [28, 33], a simple primitive-based prediction technique to model human gait was proposed. These, however, do not incorporate the mutual coupling effects between different human body parts. Another technique that has been employed is an iterative physical optics approach [34], which accounts for mutual coupling effects and can be useful only at very high frequencies, such as W-band. A full wave technique, such as the one employed in this paper, provides better accuracy for more complex structures but requires a large number of computational resources. In [35], a realistic human mesh-based model is proposed with a radar signature modeling based on Finite Difference Time Domain (FDTD) technique. However, FDTD requires a fine mesh in the order of $\lambda/50$ for accurate modeling of curved objects, which becomes prohibitive for electrically large objects such as the human [36].

In this paper, a full wave technique, namely Method of Moments enhanced with Fast Multipole Method (MoM-FMM) is used to model the walking human. This enables the accurate computation of mutual coupling effects between the different moving body parts. Ground effects are also accounted for. Furthermore, the attenuation of the incident and scattered fields as they propagate inside the medium are also taken into consideration.

MoM-FMM is an efficient numerical method which relies on grouping sources over the scatterer according to their proximity to each other. It utilizes the concept of near and far interactions, which significantly reduces the complexity of MoM from $O(N^3)$ to $O(N^{3/2})$, where N is the number of unknowns corresponding to the number of edges of the meshed object [37]. Implementing a parallelized version of this method on a high performance computing (HPC) platform provides a good speedup factor for the computation time for large-scale electromagnetic scattering problems. A brief discussion on the parallel implementation of MoM-FMM on a GPU cluster is provided below. Detailed discussions on the implementation can be found in [38, 39].

3.2.1. Parallel Implementation

The GPU cluster platform used in the implementation of this model consists of 13 computing nodes. Each node has a dual 6-core 2.66 GHz Intel Xeon processor X5650, 48 GB memory along with one Nvidia Tesla M2090 GPU running at 1.3 GHz with 6 GB of GPU memory. The nodes are interconnected through the Infiniband interconnection. The cluster populates CUDA v4.2, and MVAPICH2 v1.8.1.

The MoM-FMM algorithm consists of three main steps: pre-processing, processing, and post-processing, as shown in Figure 7. The main purpose of the pre-processing step is to read in the mesh geometry, to set up the data structure, and to divide the edges into groups. The processing step includes two phases; namely setup and linear system solution. The matrix components for near interactions, the radiation/receive functions and the translation matrix are calculated and stored in the setup phase. Iterative methods are employed for solving the linear system, and each iteration involves matrix-vector multiplications (MVM), which dominate most of the computation time. The MVM for the Z_{far} matrix comprises aggregation, translation, and disaggregation steps as depicted in Figure 7, while the MVM for the Z_{near} matrix is only an ordinary sparse matrix-vector multiplication. Finally, the post-processing step involves calculations of electromagnetics quantities of interest.

The entire processing step is implemented on GPU using the CUDA environment. To give an insight into the problem size, the scattered field calculations from a human of height 1.8 m at 5 GHz using MoM-FMM, would require 99,422 triangles for a mesh size of $\lambda/8$. This corresponds to 149,133 unknowns to be solved for using MoM-FMM. A detailed discussion on the parallel implementation of MoM-FMM on GPU clusters for larger problem sizes can be found in [39].

3.3. Forest-to-Human-to-Radar Scattering, $E_{f\text{-}h\text{-}r}$

The third contribution in the calculation of the total backscattered field at the radar, $E_{f\text{-}h\text{-}r}$, accounts for the first order interactions between the forest and human. The indirect incident fields on the human are calculated from the radiated fields from all trees in the forest towards the human. Similar to the calculation of the $E_{h\text{-}r}$ term, MoM-FMM is utilized to compute the scattered fields from the human

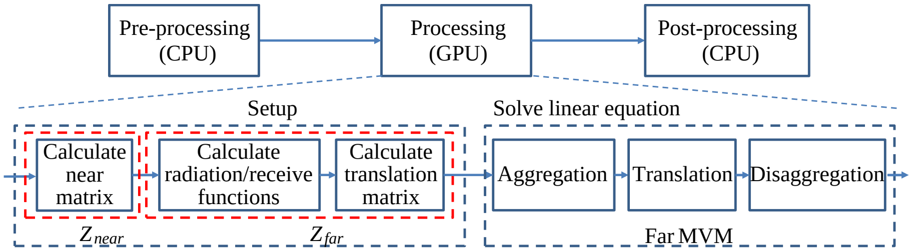

Figure 7. MoM-FMM processing step flowchart.

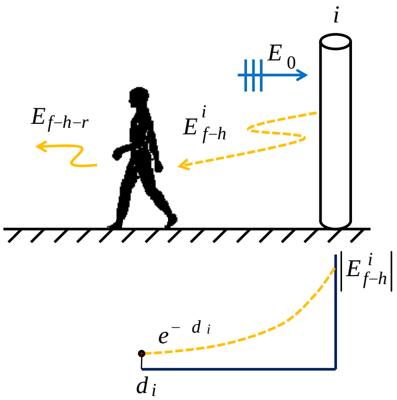

Figure 8. Forest-to-human-to-radar scattering.

based on these incident fields received from the forest. As before, ground reflections and attenuation effects are accounted for as the fields propagate inside the medium. The concept for the calculation of the $E_{f\text{-}h\text{-}r}$ term is depicted in Figure 8.

The scattered fields from each tree towards the human, $E^i_{f\text{-}h}$, is calculated by meshing each trunk into triangles and employing MoM-FMM. The induced currents on the trunk due to the incident field from the radar are computed by treating the trunk as the only scatterer in the medium. Ground reflections and attenuation effects are included as before. The induced currents on each trunk are then reradiated towards the human. The field incident on the human from each trunk, i.e., $E^i_{f\text{-}h}$, is calculated using the equivalent dipole model as reported in [40–42]. The total fields on the human are calculated by summing E^i_{f-h} for all trunks, and MoM-FMM is used to calculate $E_{f\text{-}h\text{-}r}$, i.e., the scattered field from the human due to the forest coupling.

In order to understand the mutual coupling effects between a trunk and the human, we run a few test cases as depicted in Figure 9. The three scenarios in Figure 9 correspond to the different positions of the human relative to a trunk located at the origin. In each case, the separation between the trunk and human is kept constant at 3λ, and the trunk is illuminated by a vertically polarized plane wave incident from the direction of the radar. The induced fields on the human due to the *indirect* radiation from the trunk are shown with a color map in each plot where the color red indicates the highest intensity. It should be noted that the fields on the human do not include the direct illumination by the plane wave, i.e., only the coupled fields from the trunk are shown in this figure. The relative positions of the radar, trunk and human are depicted on the right hand side for each case. Figure 9(a) corresponds to the case where the radar, trunk and human lie on the same axis, and the human is in the forward scattering

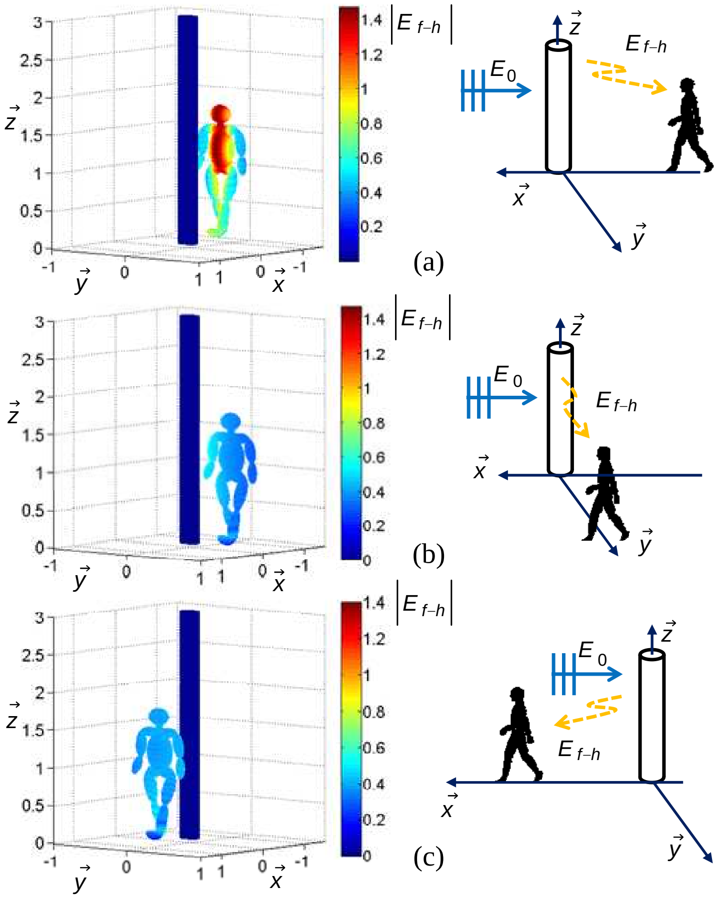

Figure 9. Induced fields on the human due to trunk for three different human positions.

direction of the trunk. The human is along the normal direction with respect to the radar-trunk axis in Figure 9(b). Finally, the human is positioned between the radar and trunk, along the radar-trunk axis, corresponding to the backscattering direction of the trunk in Figure 9(c). We observe a significant amount of field intensity on the human when it is positioned in the forward scattering direction of the trunk, i.e., Figure 9(a). The central part of the body is illuminated by stronger fields than the rest of the body for this case. In the other two cases, the illumination on the human is fairly low and more uniform.

To investigate further, we show the *total* observed field strengths with and without mutual coupling effects as a function of observation angle, φ, for the same three test cases. The fields include the total scattering from the human to radar for this investigation. Therefore, the no-coupling case corresponds to $E_{radar} = E_{h\text{-}r}$, and the coupling case represents $E_{radar} = E_{h\text{-}r} + E_{f\text{-}h\text{-}r}$. We observe that the strongest effects happen when the human is in the forward scattering direction of the trunk, i.e., Figure 10(a). The highest change in amplitude for this scenario is along the forward direction ($\varphi = 180°$). The weakest coupling contribution is observed when the human is in the backscatter direction of the trunk, i.e., Figure 10(c). There is some contribution when the human is at an orthogonal direction to the radar-trunk axis, i.e., Figure 10(b).

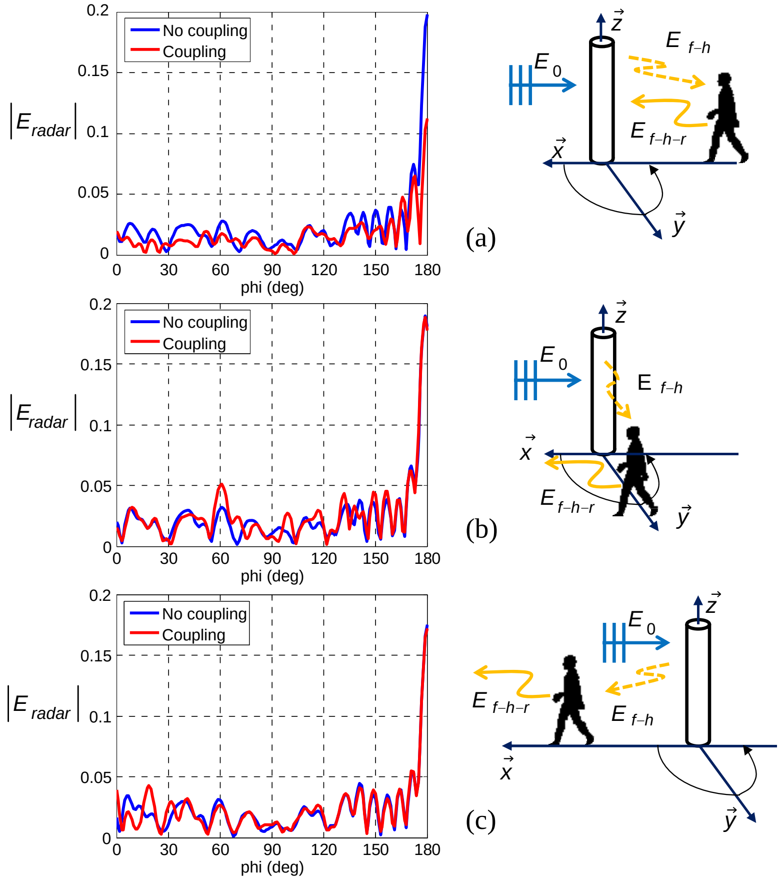

Figure 10. Comparison of mutual coupling effects for the trunk-human pair for three different human positions.

4. MICRO-DOPPLER SIGNATURE

The micro-Doppler signatures from the scene are calculated by applying a time-frequency transform, such as the Short-Time Fourier Transform (STFT) with a Gaussian window, to the scattered fields. To compute this transform, we need to choose a proper sampling rate, which depends on the maximum

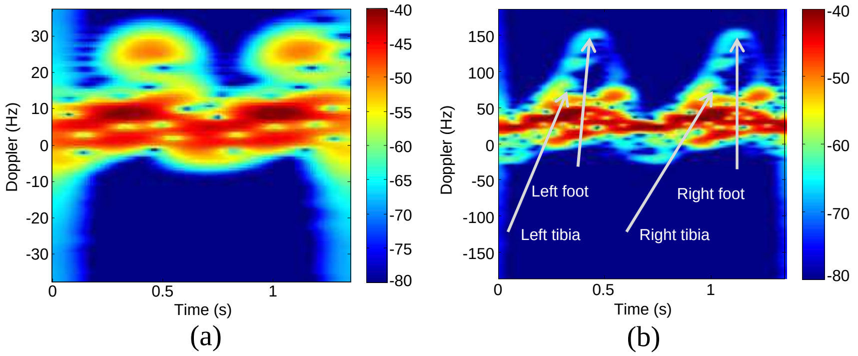

Figure 11. Spectrogram of walking human at 1 and 5 GHz.

Doppler shift. Since the Doppler shift depends on the rate of motion,v_R, i.e., $f_{Doppler} = 2v_R/\lambda_c$, the sampling rate is directly proportional to the maximum speed observed. For a maximum speed of 5 m/s, the Doppler shift can vary significantly based on the operating frequency of the radar. For instance, using a 5-GHz radar results in a Doppler shift of 166.66 Hz, which requires a sampling rate of 333.33 samples/s, while a 1-GHz radar would result in a Doppler shift of 33.33 Hz and 66.66 samples/s.

An example of a spectrogram for a human of height 1.8 m, walking at 0.9 m/s during a walking cycle of 1.346 s, along the radar's line of sight in an uncluttered environment, is shown for 1 GHz and 5 GHz in Figures 11(a) and 11(b), respectively. Based on the maximum velocity of 5 m/s, we utilize 500 samples to cover a walking cycle for 5 GHz, and 100 samples for 1 GHz. The cyclical movement of the different body parts can be observed in the spectrograms, with a significantly better resolution at 5 GHz, which clearly shows the body motion as it goes through the different phases of the walking gait as was shown in Figure 3. We observe that the responses from the different body parts are not easily distinguishable for the 1 GHz case, and higher frequencies are preferable to identify human motion in a Doppler signature.

5. SIMULATION RESULTS FROM THE SCENE

The results of our model for the micro-Doppler signatures from a moving human in a forest environment are presented in this section. A 5 GHz, z-polarized plane wave propagating along the $-\vec{x}$ direction is assumed incident on the forest, which is centered at the origin and covers an area of $40 \times 40\,\text{m}^2$ on the x-y plane as depicted in Figure 12. The circles in the figure represent the trunk positions, and the two squares denote the starting points for the human for the two paths simulated. A CW radar antenna with a half power beamwidth of 43.6 degrees is assumed to receive the scattered fields from the scene. The shaded area in Figure 12 denotes the region of the forest outside the half power beamwidth of the radar antenna. A brief description on the system parameters and a link budget calculation for the radar range are provided in Appendix A for this scenario.

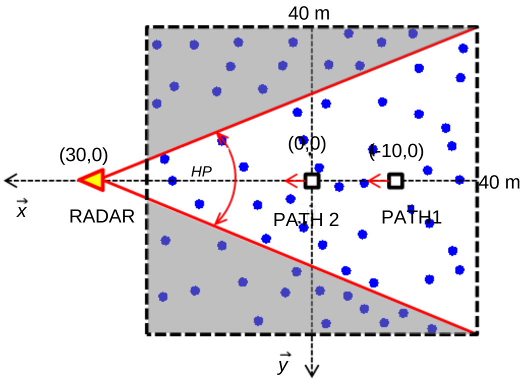

Figure 12. Simulation scenario.

A human of height 1.8 m moves with a constant speed of 0.9 m/s along the specified direct paths to radar inside the forest. The human is modeled using PEC ellipsoids, created based on the Boulic model as described in Section 2. The forest is modeled using identical trunks of 3 meters height and 11 cm radius which are distributed uniformly inside the $40 \times 40\,\mathrm{m}^2$ region. PEC is assumed for the trunk material properties as well as the ground. A trunk density of 3.8% ($\#/\mathrm{m}^2$) is assumed, which amounts to 35 trunks within the half power beamwidth of the antenna, with average closest neighbor distance of 5 m. These forest parameters are chosen to reflect the structure and spatial patterns of the trees in a typical old-growth forest [43].

The Doppler spectrogram from the scene is dependent on the path of motion with respect to the radar. To illustrate this effect, we consider two direct walking paths in the forest with different starting points as depicted in Figure 12. Path 1 starts farther away from the radar, and should be exposed to more attenuation than Path 2. Also, as a consequence of being in the back of the forest, the human following Path 1 will be in the forward scattering zone of more trees than the human in Path 2. This is expected to result in more coupling effects from the trunks. We investigate the different spectrograms for these paths in Figure 13. The same human starts with the same position and moves at the same speed for the two cases. The first step is taken with the left foot.

We observe that the motion can be detected for both scenarios, although the spectrograms differ in nature as seen in the different intensity levels for the left and right feet in Figure 13(a), while they are similar for Path 2 in Figure 13(b). The weaker signals for the left foot compared to the right foot in Figure 13(a) are due to the coupling effects experienced by the human in Path 1. We also observe that the expected attenuation effects are visible, as the signature from the path closer to the radar (Path 2) is 20 dB higher than that of Path 1. This 20 dB difference corresponds to the round trip path loss for the 10 meter separation between the two paths, based on the 1 dB/m specific attenuation assumed for the forest at 5 GHz. Another feature we notice is that, despite the attenuation, the micro-Doppler signature still reveals the human motion 30 m into the forest. Finally as expected, the static contribution from the scene is strong across the 0 Hz band for both cases, masking the lower speed motions due to the torso.

We demonstrate in Figure 14, the spectrogram from the same scene for both paths without

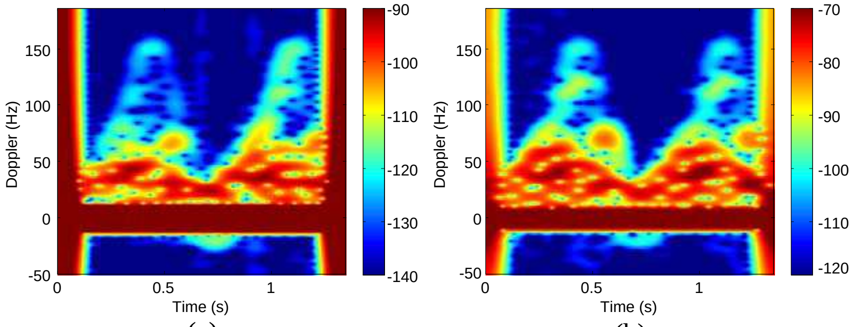

(a) (b)

Figure 13. Spectrogram for $E_{radar} = E_{f\text{-}r} + E_{h\text{-}r} + E_{f\text{-}h\text{-}r}$, for (a) Path 1 and (b) Path 2.

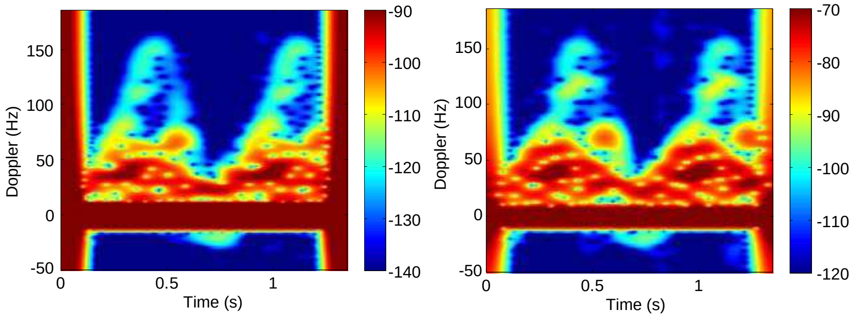

(a) (b)

Figure 14. Spectrogram for $E_{radar} = E_{f\text{-}r} + E_{h\text{-}r}$, i.e., no mutual coupling, for (a) Path 1 and (b) Path 2.

accounting for any coupling effects; i.e., neglecting the $E_{f\text{-}h\text{-}r}$ term in the total received fields at the radar. Without the mutual coupling effects, the spectrograms are now similar for the right and the left feet in both paths. We also observe that the spectrogram for Path 2 without the mutual coupling (Figure 14(b)) is very similar to the spectrogram with the coupling effects (Figure 13(b)), indicating that for this path the $E_{f\text{-}h\text{-}r}$ term was negligible. This can be explained by the fact that the human was not in the forward direction of the any of the trees closest to his path for Path 2, unlike Path 1 where the closest few trees were in the direct forward direction.

6. CONCLUSIONS

A capability to detect, track and monitor different human motions in highly cluttered environments, such as forests, is important for security and surveillance operations. In this paper we develop a model which utilizes an enhanced full wave computational technique (MoM-FMM) in combination with a first-order analytical forest model, including specific attenuation inside the forest and mutual coupling effects between the forest and the human. The solution of this large-scale electromagnetic scattering problem has been made feasible through a parallel implementation on a 13-node GPU cluster. We demonstrate that human bipedal movement is discriminable in spectrograms for a walking human in the forest.

We observe that the contribution from the forest masks the Doppler effect of the low radial velocities, which could happen depending on the path with respect to the radar or due to slow motion. Based on the specific attenuation values reported in literature for wooded areas, a CW radar at 5 GHz can discriminate the human motion as far as 30 m into the forest as observed in the spectrogram generated by our model. Also we note that the contribution from the coupling effects between human and forest is only significant if the human path is in the forward direction of the closest trees in the forest.

APPENDIX A. RADAR RANGE ESTIMATION

A brief summary of the range estimate of the system based on the radar equation, including the forest specific attenuation α as shown in Recommendation ITU-R P.833-9 [23] is presented in this Appendix. The radar equation is used to estimate the maximum operating range of our radar:

$$R_{\max} = \left(\frac{P_T G_T G_R \lambda_c^2 \sigma}{(4\pi)^3 S_{NF} \left(S/N_{\min} \right)} \right)^{1/4} \tag{A1}$$

where

P_T = transmitter output power = 60 dBm,
G_T = transmitter antenna (horn) gain = 13.3 dBi, ($\mathrm{BW}_{3\,\mathrm{dB}}$ = 43.6 deg E-plane and H-plane),
G_R = receiver antenna (horn) gain = 13.3 dBi,
λ_c = carrier frequency wavelength = 0.06 m,
σ = human body radar cross-section = 0 dBm^2,
S_{NF} = system noise floor = −130 dBm,
$S/N_{\min}$ = minimum signal-to-noise ratio = 10 dB.

Using (A1) with the parameters above, we estimate the maximum operating range of our CW radar operating at 5 GHz for human detection in free-space to be 5,406 m. For forest attenuation of 80 dB (typical specific attenuation of 1 dB/m for vertical polarization as shown in Recommendation ITU-R P.833-9 [23], along a woodland path of 40 m), the estimated maximum operating range becomes 54.3 m.

REFERENCES

1. Mencia-Oliva, B., J. Grajal, O. A. Yeste-Ojeda, G. Rubio-Cidre, and A. Badolato, "Low-cost CW-LFM radar sensor at 100 GHz," *IEEE Transactions on Microwave Theory and Techniques*, Vol. 61, No. 2, 986–998, 2013.
2. Sume, A., M. Gustafsson, M. Herberthson, A. Janis, S. Nilsson, J. Rahm, and A. Orbom, "Radar detection of moving targets behind corners," *IEEE Transactions on Geoscience and Remote Sensing*, Vol. 49, No. 6, 2259–2267, 2011.

3. Tahmoush, D. and J. Silvious, "Remote detection of humans and animals," *2009 IEEE Applied Imagery Pattern Recognition Workshop (AIPRW)*, 1–8, 2009.
4. Otero, M., "Application of a continuous wave radar for human gait recognition," *Signal Processing, Sensor Fusion, and Target Recognition XIV*, Vol. 5809, 538, Orlando, Florida, USA, Mar. 28, 2005.
5. Chen, V. C., F. Li, S.-S. Ho, and H. Wechsler, "Micro-Doppler effect in radar: Phenomenon, model, and simulation study," *IEEE Transactions on Aerospace and Electronic Systems*, Vol. 42, No. 1, 2–21, 2006.
6. Jung, J. H., U. Lee, S. H. Kim, and S. H. Park, "Micro-Doppler analysis of Korean offshore wind turbine on the L-band radar," *Progress In Electromagnetics Research*, Vol. 143, 87–104, 2013.
7. Park, J. H. and N. H. Myung, "Effective reconstruction of the rotation-induced micro-doppler from a noise-corrupted signature," *Progress In Electromagnetics Research*, Vol. 138, 499–518, 2013.
8. Pan, X., W. Wang, J. Liu, D. J. Feng, Y. Liu, and G. Wang, "Features extraction of rotationally symmetric ballistic targets based on micro-doppler," *Progress In Electromagnetics Research*, Vol. 137, 727–740, 2013.
9. Kim, Y. and H. Ling, "Human activity classification based on micro-Doppler signatures using a support vector machine," *IEEE Transactions on Geoscience and Remote Sensing*, Vol. 47, No. 5, 1328–1337, 2009.
10. Fairchild, D. P. and R. M. Narayanan, "Classification and modeling of human activities using empirical mode decomposition with S-band and millimeter-wave micro-Doppler radars," *Radar Sensor Technology XVI*, Vol. 8361, Jun. 2012.
11. Lin, A. and H. Ling, "Doppler and direction-of-arrival (DDOA) radar for multiple-mover sensing," *IEEE Transactions on Aerospace and Electronic Systems*, Vol. 43, No. 4, 1496–1509, 2007.
12. Li, C., J. Ling, J. Li, and J. Lin, "Accurate Doppler radar noncontact vital sign detection using the RELAX algorithm," *IEEE Transactions on Instrumentation and Measurement*, Vol. 59, No. 3, 687–695, 2010.
13. Zhou, Q., J. Liu, A. Host-Madsen, O. Boric-Lubecke, and V. Lubecke, "Detection of multiple heartbeats using Doppler radar," *2006 IEEE International Conference on Acoustics, Speech and Signal Processing, ICASSP 2006 Proceedings*, Vol. 2, II, 2006.
14. Chen, Y. F., D. Misra, H. Wang, H.-R. Chuang, and E. Postow, "An X-band microwave life-detection system," *IEEE Transactions on Biomedical Engineering*, Vol. 33, No. 7, 697–701, 1986.
15. Chen, Y. F., Y. Huang, J. Zhang, and A. Norman, "Microwave life-detection systems for searching human subjects under earthquake rubble or behind barrier," *IEEE Transactions on Biomedical Engineering*, Vol. 47, No. 1, 105–114, 2000.
16. Silvious, J., J. Clark, T. Pizzillo, and D. Tahmoush, "Micro-Doppler phenomenology of humans at UHF and Ku-band for biometric characterization," *SPIE Defense, Security, and Sensing*, 73080X–73080X-9, 2009.
17. Chen, V. C., "Detection and analysis of human motion by radar," *IEEE Radar Conference, RADAR' 08*, 1–4, 2008.
18. Li, J., X. Zhu, P. Stoica, and M. Rangaswamy, "High resolution angle-doppler imaging for MTI radar," *IEEE Transactions on Aerospace and Electronic Systems*, Vol. 46, No. 3, 1544–1556, 2010.
19. Armstrong, B. and B. S. Holeman, "Target tracking with a network of Doppler radars," *IEEE Transactions on Aerospace and Electronic Systems*, Vol. 34, No. 1, 33–48, 1998.
20. Thayaparan, T., L. Stankovi, and I. Djurovi, "Micro-Doppler-based target detection and feature extraction in indoor and outdoor environments," *Journal of the Franklin Institute*, Vol. 345, No. 6, 700–722, 2008.
21. Geisheimer, J. L., W. S. Marshall, and E. Greneker, "A continuous-wave (CW) radar for gait analysis," *Conference Record of the Thirty-Fifth Asilomar Conference on Signals, Systems and Computers*, Vol. 1, 834–838, 2001.
22. Mobasseri, B. G. and M. G. Amin, "A time-frequency classifier for human gait recognition," *Proc. of SPIE*, Vol. 7306, 730628, 2009.
23. ITU-R, "Attenuation in vegetation," Recommendation ITU-R, 833-8, ITU Radiocommunication

Bureau, Geneva, Switzerland, 2013.

24. Müller, M., T. Röder, M. Clausen, B. Eberhardt, B. Krüger, and A. Weber, "Documentation mocap database HDM05," Technical Report No. CG-2007-2, ISSN 1610-8892, Universität Bonn, 2007.
25. Boulic, R., N. Thalmann, and D. Thalmann, "A global human walking model with real-time kinematic personification," *The Visual Computer*, Vol. 6, No. 6, 344–358, 1990.
26. Chen, V. C., "Doppler signatures of radar backscattering from objects with micro-motions," *IET Signal Processing*, Vol. 2, No. 3, 291–300, 2008.
27. Ram, S. S. and H. Ling, "Analysis of microDopplers from human gait using reassigned joint time-frequency transform," *Electronics Letters*, Vol. 43, No. 23, 2007.
28. Van Dorp, P. and F. C. A. Groen, "Human walking estimation with radar," *IEE Proceedings — Radar, Sonar and Navigation*, Vol. 150, No. 5, 356–365, 2003.
29. Picard, G. and T. L. Toan, "A multiple scattering model for C-band backscatter of wheat canopies," *Journal of Electromagnetic Waves and Applications*, Vol. 16, No. 10, 1447–1466, 2002.
30. Lang, R. H. and J. S. Sighu, "Electromagnetic backscattering from a layer of vegetation: A discrete approach," *IEEE Transactions on Geoscience and Remote Sensing*, Vol. 21, No. 1, 62–71, 1983.
31. Tsang, L., K. Ding, G. Zhang, C. C. Hsu, and J. Kong, "Backscattering enhancement and clustering effects of randomly distributed dielectric cylinders overlying a dielectric half space based on Monte-Carlo simulations," *IEEE Transactions on Antennas and Propagation*, Vol. 43, No. 5, 488–499, 1995.
32. Tsang, L., J. A. Kong, K. Ding, and C. O. Ao, *Scattering of Electromagnetic Waves, Numerical Simulations,* John Wiley & Sons, 2004.
33. Ram, S. S., C. Christianson, Y. Kim, and H. Ling, "Simulation and analysis of human micro-Dopplers in through-wall environments," *IEEE Transactions on Geoscience and Remote Sensing*, Vol. 48, No. 4, 2015–2023, 2010.
34. Vahidpour, M. and K. Sarabandi, "Millimeter-wave Doppler spectrum and polarimetric response of walking bodies," *IEEE Transactions on Geoscience and Remote Sensing*, Vol. 50, No. 7, 2866–2879, 2012.
35. Dogaru, T. and C. Le, "Time-frequency analysis of a moving human doppler signature," ARL-TR-4728, US Army Research Laboratory, Adelphi, MD, 2009.
36. Tavlove, A. and S. C. Hagness, *Computational Electrodynamics: The Finite-difference Time-domain Method,* 3rd Edition, Artech House, 2005.
37. Coifman, R., V. Rokhlin, and S. Wandzura, "The fast multipole method for the wave equation: A pedestrian prescription," *IEEE Antennas and Propagation Magazine*, Vol. 35, No. 3, 7–12, 1993.
38. Nguyen, Q., V. Dang, and O. Kilic, "Graphics processing unit accelerated fast multipole method — Fast Fourier transform," *IEEE Antennas and Propagation Society International Symposium (APSURSI 2013)*, 1882–1883, Lake Buena Vista, FL, USA, Jul. 7–12, 2013.
39. Nguyen, Q. M., V. Dang, O. Kilic, and E. El-Araby, "Parallelizing fast multipole method for large-scale electromagnetic problems using GPU clusters," *IEEE Antennas and Wireless Propagation Letters*, Vol. 12, 868–871, 2013.
40. Rao, S. M., D. Wilton, and A. W. Glisson, "Electromagnetic scattering by surfaces of arbitrary shape," *IEEE Transactions on Antennas and Propagation*, Vol. 30, No. 3, 409–418, 1982.
41. Leat, C. J., N. V. Shuley, and G. F. Stickley, "Triangular-patch model of bowtie antennas: Validation against Brown and Woodward," *IEE Proceedings — Microwaves, Antennas and Propagation*, Vol. 145, No. 6, 465–470, 1998.
42. Makarov, S., *Antenna and EM Modeling with MATLAB*, Princeton University Press, 2002.
43. Chokkalingam, U. and A. White, "Structure and spatial patterns of trees in old-growth northern hardwood and mixed forests of northern Maine," *Plant Ecology*, Vol. 156, No. 2, 139–160, 2001.